

Kleban, E., Jones, D. K., & Tax, C. M. W. (2023). The Impact of Head Orientation with Respect to B_0 on diffusion tensor MRI Measures. *Imaging Neuroscience*, Advance Publication. https://doi.org/10.1162/imag_a_00012

The Impact of Head Orientation with Respect to B_0 on diffusion tensor MRI measures

Elena Kleban^{1,2}, Derek K Jones^{1,3}, Chantal MW Tax^{4,5}

¹CUBRIC, School of Psychology, Cardiff University, Cardiff, UK

²Inselspital, University of Bern, Bern, Switzerland

³MMIHR, Faculty of Health Sciences, Australian Catholic University, Melbourne, Australia

⁴CUBRIC, School of Physics and Astronomy, Cardiff University, Cardiff, UK

⁵UMC Utrecht, Utrecht University, Utrecht, The Netherlands

Abstract

Diffusion tensor MRI (DT-MRI) remains the most commonly used approach to characterise white matter (WM) anisotropy. However, DT estimates may be affected by tissue orientation w.r.t. \vec{B}_0 due to local gradients and intrinsic T_2 orientation dependence induced by the microstructure. This work aimed to investigate whether and how diffusion tensor MRI-derived measures depend on the orientation of the head with respect to the static magnetic field, \vec{B}_0 . By simulating

WM as two compartments, we demonstrated that compartmental T_2 anisotropy can induce the dependence of diffusion tensor measures on the angle between WM fibres and the magnetic field. In *in vivo* experiments, reduced radial diffusivity and increased axial diffusivity were observed in white matter fibres perpendicular to \vec{B}_0 compared to those parallel to \vec{B}_0 . Fractional anisotropy varied by up to 20% as a function of the angle between WM fibres and the orientation of the main magnetic field. To conclude, fibre orientation w.r.t. \vec{B}_0 is responsible for up to 7% variance in diffusion tensor measures across the whole brain white matter from all subjects and head orientations. Fibre orientation w.r.t. \vec{B}_0 may introduce additional variance in clinical research studies using diffusion tensor imaging, particularly when it is difficult to control for (e.g. fetal or neonatal imaging, or when the trajectories of fibres change due to e.g. space occupying lesions).

Keywords: Diffusion Tensor Imaging, Magnetic Resonance Imaging, Transverse relaxation, orientation anisotropy, fibre direction

1. Introduction

MRI can provide invaluable information on tissue composition and structure *in vivo* through the manipulation of spins with magnetic fields. Several MRI

contrasts have shown a dependence on tissue orientation w.r.t. the main magnetic field direction (\vec{B}_0), including $T_2^{(*)}$, T_1 , and magnetisation transfer [1–19]. Orientation-dependence of the apparent $T_2^{(*)}$ in adult white matter (WM) has primarily been attributed to local magnetic susceptibility-induced gradients from the myelin sheath, and as such can provide valuable information on its condition in health and disease [10, 19]. In addition, recent work [20] found that orientational anisotropy of transverse relaxation rates in newborn WM, with a much lower degree of myelination, followed the pattern of residual dipolar coupling. Recent works have demonstrated different orientational behaviours of T_2 -estimates in intra- and extra-axonal microstructural WM compartments [21, 22], see also Appendix A.

In diffusion MRI (dMRI) typically only the orientation-dependence on externally applied spatial gradients is considered: it sensitises the signal to the diffusion of water molecules in one or multiple directions by deliberately applying magnetic field gradients, and as such can infer information on the directional organisation of tissue. At low to moderate diffusion weightings, the diffusion tensor MRI (DT-MRI) representation [23] remains the most commonly used approach to characterise the diffusion process, and DT-MRI-derived measures such as mean diffusivity (MD) and fractional anisotropy (FA) reflect both intra- and extra-axonal signal contributions.

Theoretically, dMRI signals and derived measures can also exhibit \vec{B}_0 -orientation dependence when magnetic susceptibility variation is combined with anisotropic geometry at a subvoxel level. Several mechanisms may contribute to dMRI-signal-anisotropy in this case. Firstly, several works have considered the interaction (or cross-term) of susceptibility-induced gradients with the externally applied diffusion encoding gradients, and their effect on estimates of the apparent diffusion coefficient (ADC) [15, 24–29]. Specifically, local gradients in the direction of the diffusion encoding gradient can lead to an under- or overestimation of ADC from individual isochromats, leading to a reduction of the overall ADC because isochromats with reduced ADC contribute a higher weighting [24]. By employing sequences sensitive and insensitive to local susceptibility-induced gradients, early *ex vivo* experiments in WM [26, 30] concluded that the effects from local gradients on diffusivity values did not have a measurable role in nerve samples at 4.7T and 2.35T, respectively, which was later corroborated *in vivo* at 1.5T [27]. Interestingly, [26] did observe that diffusivity values along the axon varied by about 15% due to reorientation w.r.t. \vec{B}_0 . *In silico* works provided theoretical background on the effect of mesoscopic susceptibility on ADC and DT-derived measures under variable diffusion times [29] and sample orientation [15], respectively. Furthermore, the recent observation of differences in compartmental T_2 -anisotropy suggests

another mechanism of \vec{B}_0 -orientation dependence in DT-measures. The intrinsic T_2 -weighting of the diffusion-weighted spin-echo sequence affects the T_2 -weighting of intra- and extra-axonal signal fractions. As a result, differences in compartmental T_2 -orientation dependence w.r.t. \vec{B}_0 can lead to orientation-dependent variation in compartmental signal fractions and, consequently, affect DT-measures.

This motivates further investigation of the potential orientational dependence of DT measure w.r.t. \vec{B}_0 . The additional dMRI dependence on tissue-orientation w.r.t. \vec{B}_0 may introduce variability in the results when not taken into account, potentially reducing statistical power to detect true effects, and could even provide important additional information on tissue microstructure (e.g. myelin). The aim of this work is to determine the variation of DT-MRI-derived measures as a function of fibre orientation w.r.t. \vec{B}_0 . To this end, we investigate the effect of head-orientation dependence of compartmental T_2 [21] and the consequent variation of compartmental signal fractions on DT-MRI measures *in silico*, and characterise the \vec{B}_0 -orientation dependence in *in vivo* human brain data at 3 T using a tiltable RF coil.

2. Methods

2.1. Simulations

The following simple simulations investigate the effect of \vec{B}_0 -orientation dependence of compartmental T_2 [21] on estimated DT-MRI measures, thereby not considering cross terms between the diffusion and background gradient. The simulations are based on a ‘standard model’ of diffusion for white matter in the long-time limit, which models the intra-axonal space as a ‘stick’ with zero perpendicular apparent diffusivity and the extra-axonal space as axially symmetric tensor [31–34]. Different levels of complexity are investigated: First, in the case of no fibre dispersion and no noise, one can derive analytical equations for the ADC as a function of compartmental diffusivities, signal fractions, and compartmental T_2 (which can be \vec{B}_0 -orientation dependent). Second, still in the case of no dispersion, the signal can be generated from analytical equations, noise added, and the DT fitted. Finally, this can be repeated for signals generated in the case of fibre dispersion.

For all simulations, scenarios for a range of θ (i.e., orientation w.r.t. \vec{B}_0) were generated corresponding to the distribution of θ observed in the *in vivo* data of all subjects and head orientations (see section 2.2).

Analytical case: no dispersion and no noise. Consider a simplified two-compartment model of the diffusion- and T_2 relaxation-weighted signal in WM (no fibre dispersion) as a function of the echo time, TE, and b -value:

$$S(b, \mathbf{g}, \text{TE}) = f \cdot e^{-R_{2,ia}\text{TE}} \cdot e^{-b\mathbf{g}^T \mathbf{D}_{ia} \mathbf{g}} + (1 - f) \cdot e^{-R_{2,ea}\text{TE}} \cdot e^{-b\mathbf{g}^T \mathbf{D}_{ea} \mathbf{g}}, \quad (1)$$

where subscripts i/e denote intra-/extra-axonal compartments, respectively, $R_2 = 1/T_2$ are the relaxation rates, \mathbf{D} are positive semi-definite diffusion tensors, and f is intra-axonal signal fraction. Suppose \mathbf{D}_{ia} and \mathbf{D}_{ea} have equal principal eigenvectors (denoted by \mathbf{n}) and parallel and perpendicular eigenvalues $D_{ia,\parallel}, D_{ia,\perp}$ (where $D_{ia,\perp} = 0$) and $D_{ea,\parallel}, D_{ea,\perp}$ respectively, then the signal can be simplified as

$$S(b, \mathbf{g}, \text{TE}) \sim f \cdot e^{-R_{2,ia}\text{TE}} \cdot e^{-bD_{ia}} + (1 - f) \cdot e^{-R_{2,ea}\text{TE}} \cdot e^{-bD_{ea}}, \quad (2)$$

where $D = D_{\perp} + (\mathbf{g} \cdot \mathbf{n})^2(D_{\parallel} - D_{\perp})$.

Considering DTI as a signal representation at sufficiently low b -values, i.e. capturing the first order b -term in the Cumulant expansion [35], one can derive

expressions for the ADC, e.g. by expanding in powers of b the analytic expression for $\ln S(b)$ (Eq. 2). For non-interacting compartments, the diffusion coefficient is a weighted sum of the diffusivities in the individual compartments where the signal fractions are T_2 -weighted. Specifically, the ADC is the first order term of the Maclaurin series expansion of $\ln(S)$ in b :

$$\text{ADC}(\text{TE}) = \frac{f \cdot D_{\text{ia}} \cdot e^{-R_{2,\text{ia}} \text{TE}} + (1-f) \cdot D_{\text{ea}} \cdot e^{-R_{2,\text{ea}} \text{TE}}}{f \cdot e^{-R_{2,\text{ia}} \text{TE}} + (1-f) \cdot e^{-R_{2,\text{ea}} \text{TE}}} . \quad (3)$$

Eq. 3 was used to compute apparent axial diffusivity (AD, $\mathbf{g} \parallel \mathbf{n}$), radial diffusivity (RD, $\mathbf{g} \perp \mathbf{n}$), MD, and FA. Recent work suggests that the effect of WM fibre orientation θ to the magnetic field can most prominently be observed in the extra-axonal apparent transversal relaxation rate $R_{2,\text{ea}} = 1/T_{2\text{ea}}$ [21]. The dependence could be described as

$$R_{2,\text{ea}}(\theta) = R_{2,\text{iso}} + R_{2,\text{aniso}} \sin^4 \theta. \quad (4)$$

This orientational dependence of $R_{2,\text{ea}}(\theta)$ will result in orientational dependence of the ADC in addition to a straightforward TE dependence.

Analytical noiseless scenarios were simulated using Eq. 3 and 4. TEs were

selected to match the *in vivo* acquisition (cf., section 2.2.1). The axonal fraction was varied $f = [0.1, 0.3, 0.5, 0.7, 0.9]$ and diffusivities D and relaxation rates R_2 were set to the following values: $[D_{i,\parallel}, D_{e,\parallel}, D_{e,\perp}] = [2.6, 2, 0.4] \mu\text{m}^2/\text{ms}$, and $R_{2,i} = 12 \text{ [s}^{-1}\text{]}$, $R_{2,e} = 17.4 + 2.4 \cdot \sin^4\theta \text{ [s}^{-1}\text{]}$, respectively.

Noise simulations without dispersion. Eq. 2 was used to simulate signals with TE, b and \mathbf{g} matching the *in vivo* data section 2.2. Signals were simulated using the same fractions, intra- and extra-axonal diffusivities and relaxation rates as for the analytical simulations. Rician noise was added to the signal with an SNR of 100 on the $b = 0, TE = 0$ signal, similar to the *in vivo* acquisitions [21]. DT were estimated for each TE on $b \leq 1500 \text{ s/mm}^2$ data using iterative weighted linear least squares, and AD, RD, MD, and FA were computed.

Noise simulations with dispersion. Finally, the effect of fibre orientation dispersion was studied by forward simulating a distribution of orientation-dispersed compartments according to a Watson distribution, where each sub-compartment (i.e. each distinctly oriented extra-axonal compartment) can separately exhibit R_2 -orientation dependence [21, Appendix A]. Tissue properties, noise, and estimation were as described in the simulations without dispersion.

Data analysis. To quantify the magnitude of orientation dependence, B , the simulated values of each DTI-derived measure at each TE were directly represented by a function of θ :

$$F(\theta) = A + B \cdot \sin^4\theta . \quad (5)$$

We note that this representation does not exactly describe the orientation dependence even in the simplest analytical case (Eq. 3), but nevertheless provides a close approximation (see an example of a $\sin^4\theta$ -fitting in supporting Figure S1) and allows for the quantification of anisotropy through the estimation of B . The performance of the anisotropic representation relative to the isotropic case, $F(\theta) = A$, was estimated using the rescaled Akaike's Information Criterion (AIC) [36, 37]: $\Delta_{\text{AIC}} = \text{AIC} - \text{AIC}_{\text{min}}$. Here, AIC_{min} is the minimal AIC value in the set. Per [37], Δ_{AIC} values allow comparison of the relative merits of representations in the set as follows: representations having $\Delta_{\text{AIC}} \leq 2$ are considered to have similar substantial support as the representation with AIC_{min} , those with $4 \leq \Delta_{\text{AIC}} \leq 7$ have considerably less evidence, and those with $\Delta_{\text{AIC}} \geq 10$ have no support. Additionally, the isotropic model is selected over the anisotropic, if the 85% confidence interval of the magnitude of anisotropy included zero [38].

2.2. *In vivo* data

In this work we used a subset of the multi-dimensional diffusion- R_2 data presented in previous work [21], relevant data acquisition and pre-processing steps are re-iterated below. The study was approved by the Cardiff University School of Psychology Ethics Committee and written informed consent was obtained from all participants in the study.

2.2.1. Data acquisition.

Multi-dimensional diffusion- R_2 -weighted data were acquired from five healthy participants (3 female, 25-31 y.o.) on a 3 T MRI scanner equipped with a 300 mT/m gradient system and a 20ch head/neck receive coil that can tilt about the L-R axis (Siemens Healthineers, Erlangen, Germany). The acquisition was repeated in default (0°) and tilted (18°) coil-orientation to introduce variable anatomical orientation w.r.t. \vec{B}_0 . Acquisition parameters are summarised in Figure 1A.

2.2.2. Data processing.

The data were checked for slice-wise outliers [39] and signal drift, corrected

for Gibbs ringing [40], subject motion, geometrical distortions [41–43] and noise bias [44–47].

From the pre-processed data a subset with diffusion weightings matching across echo times was selected (Figure 1B), and for each echo time diffusion tensors, fibre orientation w.r.t. \vec{B}_0 and single fibre population masks were obtained as described below. DT were estimated for each TE on the nominal $b = [0, 750, 1500]$ s/mm² data, using iterative weighted linear least squares. Gradient non-linearities were considered and b -values/-vectors were corrected correspondingly prior to fitting [48]. Fibre orientations θ w.r.t. \vec{B}_0 were computed from the first eigenvector of the estimated DT. Note that \vec{B}_0 has to be in image coordinates of each subject/head orientation.

Fibre orientation distribution functions (fODF) [49, 50] were estimated per TE using multi-shell multi-tissue constrained spherical deconvolution [51] from the data acquired at TE = 54 ms. From the fODFs single-fibre population (SFP) voxels with low dispersion ($p_2 > 0.5$) were identified [52]. Dispersion was quantified by $p_2 = \sqrt{4\pi/5} \sqrt{\sum_m |p_{2m}|^2}$, where p are spherical harmonics coefficients [21, 53, 54].

We used WM tract segments extracted in previous work [21]. Briefly, 18 major WM tracts and, where applicable, their bilateral counterparts were extracted and segmented using TractSeg [55].

2.2.3. Data analysis.

θ -dependence of DT measures: pooling all SFP voxels. General trends in orientational anisotropy of DTI measures were investigated by subdividing the range of angles into bins, averaging the estimates within each bin, and smoothing. Specifically, the data were binned in 1° -subsets and the corresponding DT-measure estimates and θ -values were averaged across each bin, denoted as $\langle \text{measure} \rangle_{1^\circ}$ and $\langle \theta \rangle_{1^\circ}$. Then, a smoothing spline as a function of $\langle \theta \rangle_{1^\circ}$ and weighted by the number of data points in each bin was fitted to $\langle \text{measure} \rangle_{1^\circ}(\langle \theta \rangle_{1^\circ})$. An example of this procedure is shown in supporting Figure S2 for the lowest TE.

The magnitude of anisotropy was defined as the difference between the minimal and the maximal values of the fitted curves. Their signs were set negative if the minimal values were below those at $\theta = 0$. The contribution of orientational anisotropy to overall variance was calculated as: $(\text{std}_{\text{iso}} - \text{std}_{\text{aniso}})/\text{std}_{\text{iso}}$. Here, $\text{std}_{\text{aniso}}$ and std_{iso} are the standard deviations across all SFP voxels with and

without orientational anisotropy being considered, respectively. Additionally, mean values A across all SFP voxels were obtained for each measure and TE.

In addition to the spline-analysis, to assess whether DT measures as a function of θ showed significant orientation-dependence, we assessed whether an anisotropic representation described the data better than isotropic (cf., Supporting Information), using the approach similar to the *in silico* analysis described in section 2.1.

θ -dependence of DT measures: tractometry analysis to achieve spatial correspondence. By comparing the measures estimated within the same anatomical region at default or tilted coil orientation, we aimed to reduce the effects of the potential microstructural variability across the WM in the approach described above. The anatomical correspondence between the coil-orientations was established using the segments derived from the tractometry approach. The outer-most 20% of tract segments and the segments with 3 or fewer voxels were excluded to minimise the effects of fanning and noise, respectively. To obtain the effect of the re-orientation we evaluated $\langle \text{measure}_{0^\circ} \rangle^S - \langle \text{measure}_{18^\circ} \rangle^S$ as a function of $\langle \sin^4 \theta_{0^\circ} \rangle^S - \langle \sin^4 \theta_{18^\circ} \rangle^S$. Here, $\langle \rangle^S$ denotes the average of corresponding values from SFP voxels over each segment, and the subscripts 0° and 18° correspond to default and tilted

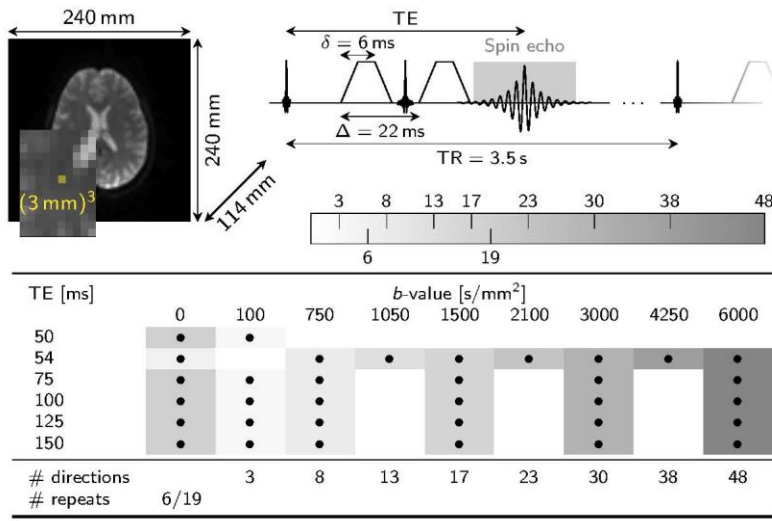
head-orientations, respectively.

3. Results

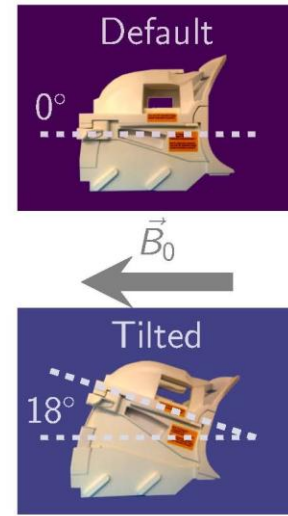
3.1. Simulations

Figure 2AB shows examples of MD, AD, RD, and FA as a function of fibre orientation θ to \vec{B}_0 for the noiseless analytical simulations without fibre dispersion. For the parameter settings investigated, AD and FA increase with θ (the magnitude of anisotropy, $\hat{B} > 0$), while RD decreases ($\hat{B} < 0$). The absolute value of the magnitude of anisotropy, $|\hat{B}|$, generally increases with TE. The resulting behaviour of MD is non-trivial and sensitive to simulation parameters (e.g., axonal signal fraction f), with possible sign flips of \hat{B} for increasing TE.

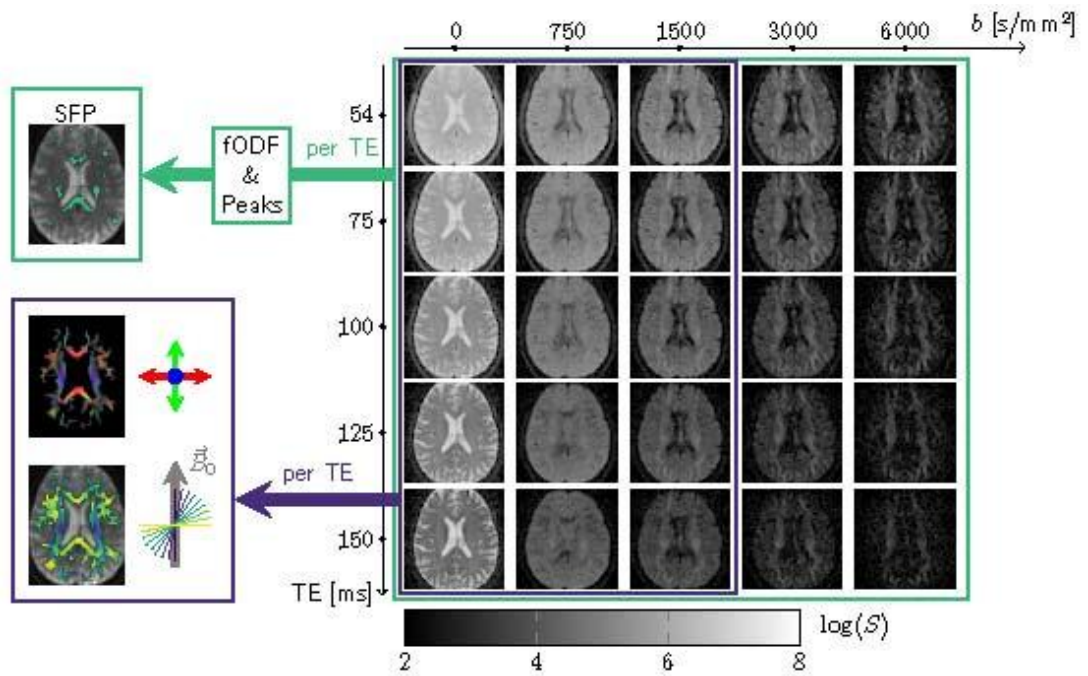
R_2 -diffusion correlation experiment



Head reorientation



A. Multi-dimensional R_2 -diffusion data were acquired under simultaneous modulation of echo times and diffusion-gradient amplitudes in a pulsed-gradient spin-echo sequence with EPI readout. Time between diffusion gradients, $\Delta = 22 \text{ ms}$, and diffusion gradient duration, $\delta = 8 \text{ ms}$, were kept fixed for all echo times. The gradient orientations were defined in scanner coordinates and thus were not rotated with the head re-orientation. Additional modulation of fibre orientation was achieved by head re-orientations relative to \vec{B}_0 .



B. A subset of the pre-processed multi-dimensional diffusion- R_2 -weighted dataset from previous work[21] was used to calculate echo-time-dependent diffusion tensors and fibre orientation to B_0 (denoted by θ) (blue, bottom left), and single-fibre-population (SFP) voxels (green, top left).

Figure 1: Methods

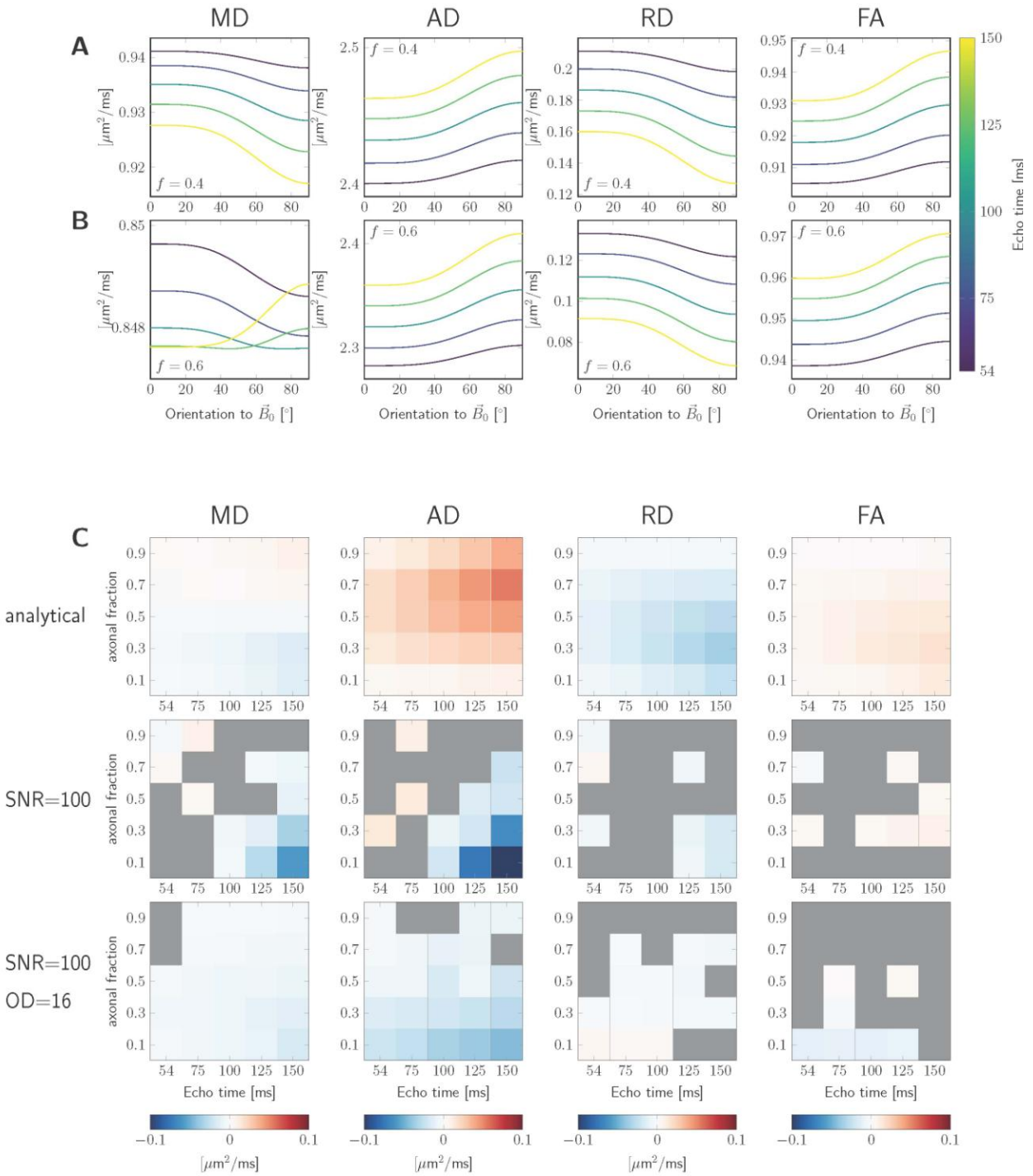
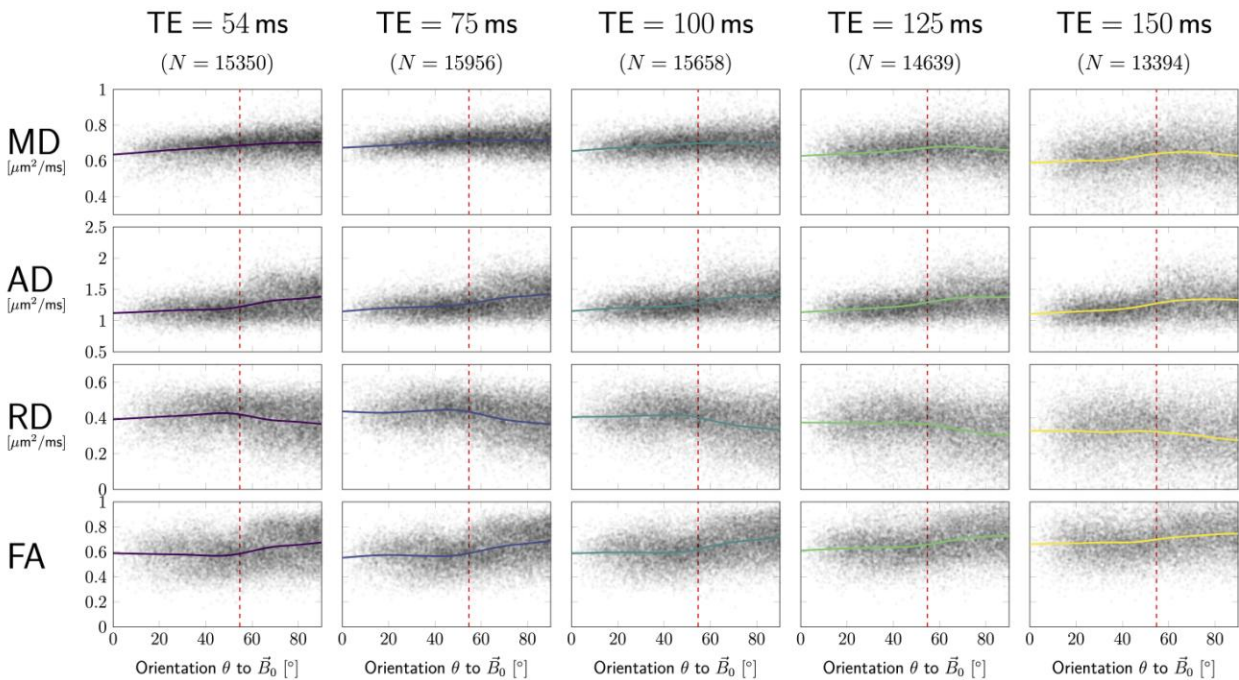
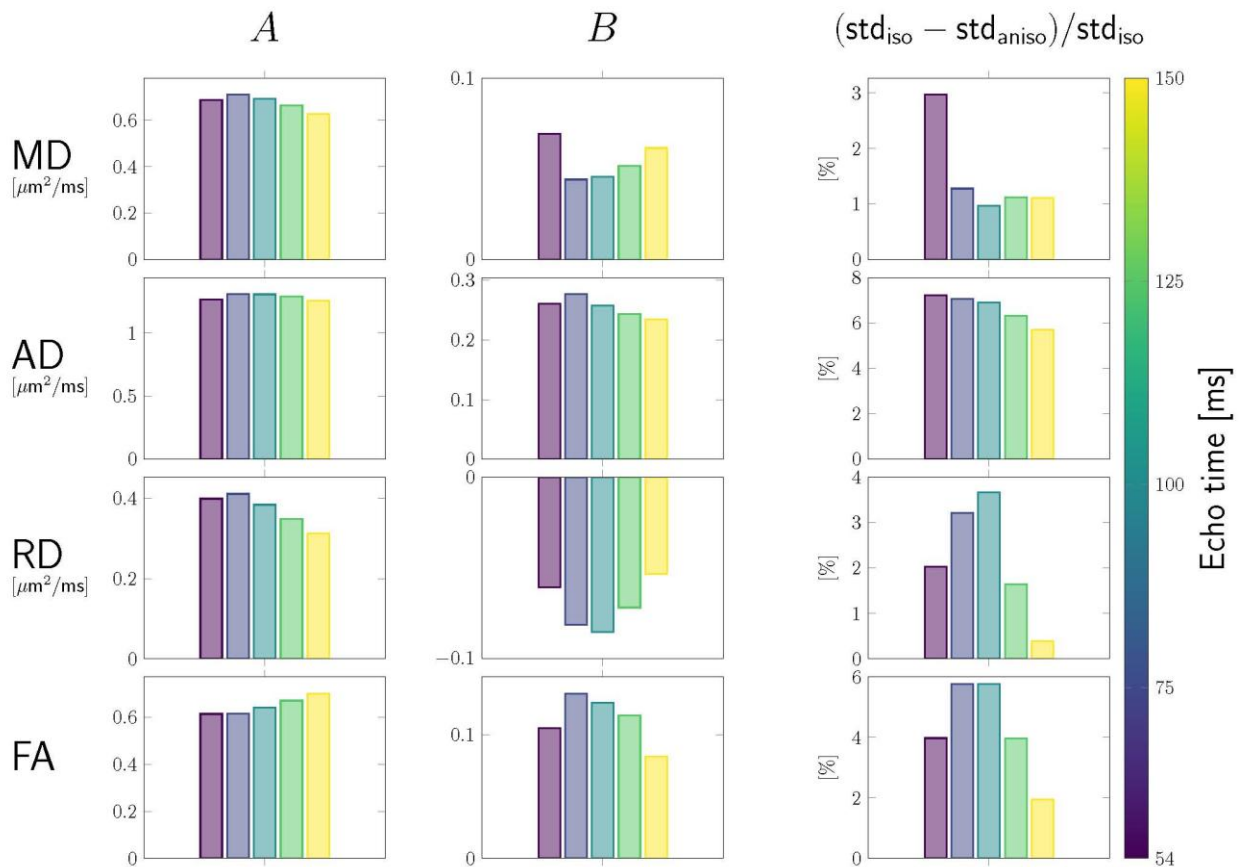


Figure 2: **Simulation results.** The signals were estimated for variable echo times and axonal fractions, f , and fixed diffusivities $[D_{i,\parallel}, D_{e,\parallel}, D_{e,\perp}] = [2.6, 2, 0.4] \mu\text{m}^2/\text{s}$

ms, and relaxation rates $R_{2,i} = 12$, $R_{2,e} = 17.4 + 2.4 \cdot \sin^4\theta$. Figures in **A.** and **B.** were estimated analytically (Equations 3 and 4) and show MD, AD, RD, and FA as functions of fibre orientation w.r.t. \vec{B}_0 for $f = 0.4$, and $f = 0.6$, respectively. In **C.** the magnitude of anisotropy, B , (colors) is shown as a bi-modal function of the echo time (horizontal axis) and the axonal fraction (vertical axis, $f = [0.1,0.3,0.5,0.7,0.9]$). Columns left-to-right are different DTI measures: MD, AD, RD, FA; rows top-to-bottom are different simulation conditions: using the analytical expression, assuming noisy signal with $\text{SNR} = 100$, and adding fibre dispersion ($\text{OD} = 16$) in addition to noise, respectively.



A. Each DTI measure (rows) from SFP voxels was plotted against the fibre orientation, θ , to the magnetic field. Each column/colour corresponds to a different TE. Solid lines represent best fitting smoothing spline curves. Dashed red lines indicate the magic angle of 54.7° .



B. The estimated mean value, A , and the magnitude of anisotropy, B , over all SFP voxels are shown in the first and the second column, respectively. Third column shows the amount of decrease in variation of values when orientation w.r.t. \vec{B}_0 is

taken into account. Colours represent the corresponding echo times, for which anisotropy of the measures was investigated.

Figure 3: **Pooled SFP data results.**

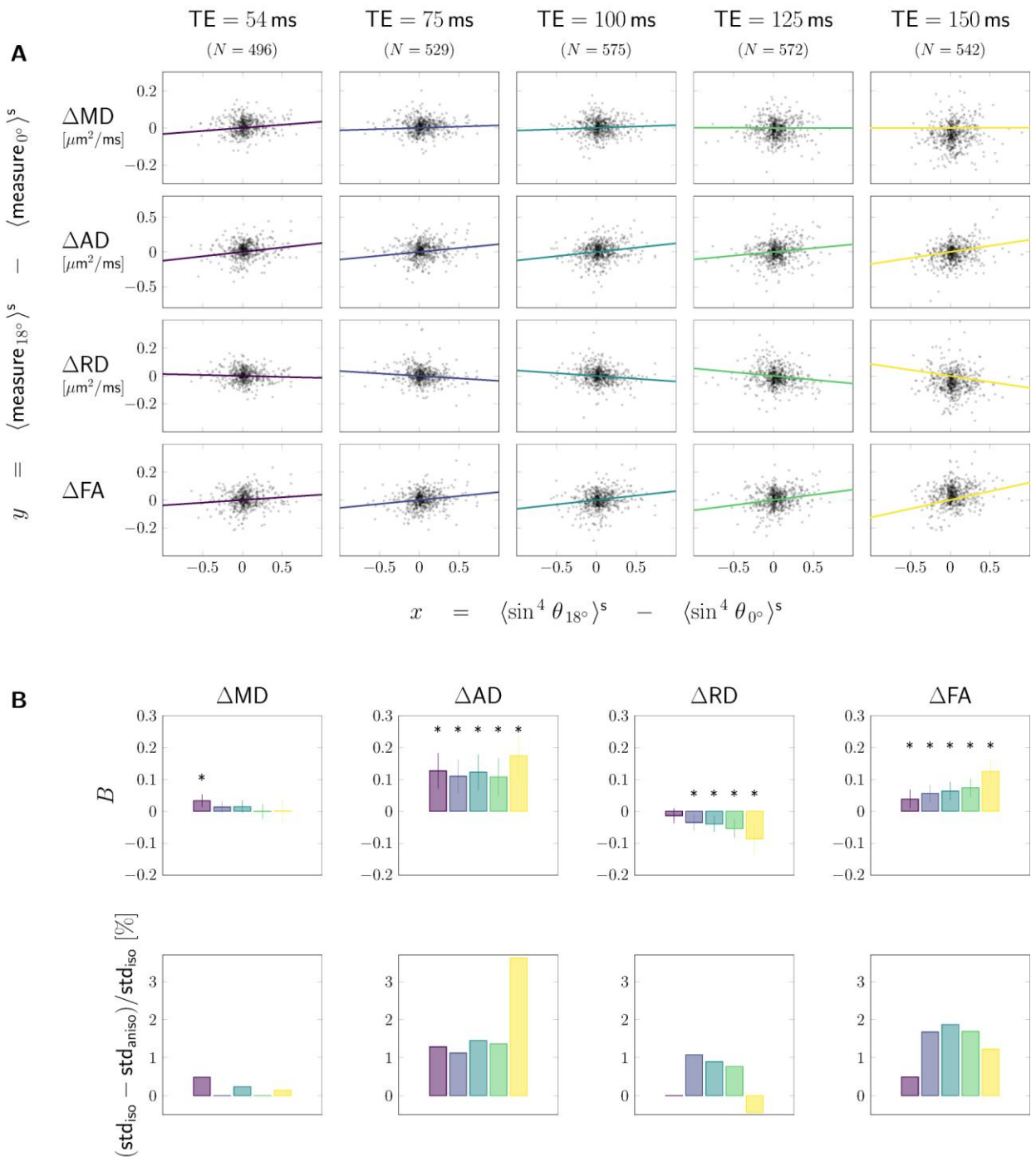


Figure 4: **Tractometry results.** Tractometry was used to achieve anatomical correspondence between tilted and default head orientation, by comparing values of DTI-measures in default vs tilted head orientations tract- and segment-wise. **A.** In

scatterplots, changes in value of the respective DTI measure with re-orientation (rows) are plotted as a function of the corresponding change in $\sin^4\theta$. **B.** Barplots show: the magnitude of anisotropy estimated for each DTI measure and each echo time (top row); and the change in standard deviation (std) when fibre anisotropy is taken into account (bottom row). Data in which anisotropic representation ($y = B \cdot x$) described the data better ($AIC_{\text{iso}} - AIC_{\text{aniso}} > 2$) than isotropic assumption ($B = 0$) were indicated by a *-symbol.

Figure 2C shows results for the analytical simulations following Eq. 3 and 4 (first row), and the noisy simulations without (middle row) and with (third row) fibre dispersion. The plots show the estimated anisotropy \hat{B} (colormap) for the scenario $D_{\parallel,i} = 2.6\mu\text{m}^2/\text{ms}$, $D_{\parallel,e} = 2\mu\text{m}^2/\text{ms}$, and $D_{\perp,e} = 0.4\mu\text{m}^2/\text{ms}$, echo times matching the acquisition parameters (horizontal axis) and a range of f (vertical axis). The columns show results for different DT measures. A grey colour indicates scenarios for which an isotropic representation was favoured (section 2.2.3). It becomes immediately apparent that the effect on DT measures can be vastly different depending on the scenario: in the simple analytical simulations B for MD can either be positive (high f) or negative (low f) depending on the intra-axonal signal fraction and its absolute value becomes larger for increasing TE. For the simulation with noise and no dispersion B can be positive or negative, and in the case of

dispersion B is lower and negative in the cases investigated. For AD, B is predominantly positive in non-dispersion analytical scenario and has the largest value for high TE, but in the noisy simulations B could be negative. The behaviour of \square_{RD} is more consistent across simulation scenarios. Whereas B_{FA} is mostly positive and largest for high TE and low f in the no-dispersion noiseless and noisy cases, B can be positive or negative in the noisy scenarios but is overall low or non-significant.

3.2. *In vivo* data

Pooled data. In Figure 3A DT measures are plotted as functions of fibre orientation θ w.r.t. \vec{B}_0 (horizontal axes), and echo time TE (columns), along with the corresponding smoothing spline curves highlighting anisotropic effects. The data were pooled from all subjects and both head orientations, each data point represents one SFP voxel. RD and FA show global maxima and minima, respectively, closed to the magic angle (dashed red lines), most prominently for low TE.

The barplots in Figure 3B show the average value (A , first column) or the magnitude of anisotropy (B , second column) obtained from all SFP voxels for a

given measure (rows). MD, AD and FA increase as a function of θ ($B > 0$), while RD decreases ($B < 0$). The anisotropic component B is least dependent on the echo time for axial diffusivity. For other measures $B(\text{TE})$ is non-monotonic (for evaluated TE-s) with its absolute value being minimal (for MD) or maximal (RD, FA) at around 75-100 ms. The fibre-orientation-independent component A (first column, Figure 3B) evolves non-monotonically as a function of TE. The relative range of change of DT-measures across angles (computed as B/A , results not shown) can reach values up to 20%. Finally, column three of Figure 3B shows the fraction by which anisotropy effects contribute to overall variance, showing the largest contribution for AD (around 7% at TE = 54, ms). For MD, RD, and FA the variance contribution was 3%, 2%, and 4%, respectively, at the same shortest echo time

We also observed an overall similar behaviour in magnitude of anisotropy B when the pooled data were evaluated using $\sin^4\theta$ -representation instead of the spline-fit (cf., supporting Figure S3).

Segment-wise comparison. The scatterplots in Figure 4A show segment-wise differences between the values in tilted and default head orientation of each measure (rows) against the $\sin^4\theta$ of fibre orientations w.r.t. \vec{B}_0 . Each column

and the corresponding colour of the linear fit $y = B \cdot x$ represent different echo times. The fitting results are summarised in the top row of Figure 4B, and the fraction of variance contributed by the anisotropy effects is in the barplots of the bottom row.

Compared to the pooled analysis, the sign of anisotropy was the same (positive for MD, AD, and FA and negative for RD), but the trend as a function of TE was different for the segment-wise analysis (e.g. the magnitude of anisotropy $|B|$ in RD increased with echo time whereas the pooled analysis showed a decrease for the largest echo times).

4. Discussion

We used diffusion- T_2 -correlation data acquired in two head-orientations using a tiltable coil [21] to achieve a larger range of orientations and investigate the effect of head-orientation on diffusion tensor measures: mean, axial and radial diffusivities, and fractional anisotropy. We observed that fibre orientation w.r.t. \vec{B}_0 may be responsible for up to three, seven, and two percent of variance in MD, AD, and RD, respectively, at TE = 54 ms and about four percent of variance in FA at the same TE. We also utilised tractometry to achieve anatomical correspondence

and used the $\sin^4\theta$ -representation to estimate the effect of head-reorientation.

4.1. TE-dependence of DTI-measures.

Echo-time-dependence of diffusion coefficients and DT-derived measures has long been recognised. [56] have reported an increase/decrease of ADC with longer TE when diffusion weighting was applied parallel/perpendicular to the rat's trigeminal nerve. These are in correspondence with analytical observations visualised in e.g. Figure 2A: axial diffusivity, AD, increases, while radial diffusivity, RD, decreases with longer echo times. Assaf and Cohen [57] performed diffusion experiments with variable echo time to demonstrate the presence of two distinct diffusing compartments, they also found that the signal of the slow diffusing component has a lower R_2 relaxation rate. This, again, would correspond to the decrease in radial diffusivity with longer TE. Finally, Qin et al. [58] have explored DTI measures as functions of echo time in rhesus monkey internal capsule. They similarly reported a decrease in the radial and increase in axial diffusivities with longer TEs, but also an increase in fractional anisotropy and no significant changes to the mean diffusivity. Lin et al. [59] made similar observations for the human corpus callosum and internal capsule, in addition they observed no TE-dependence of AD in the corpus callosum.

In our data, which were pooled from WM SFP voxels, we did not observe any linear trends (cf. isotropic representation, *A*, Figure 3B), the non-monotonic variations of the DTI-measures could be due to the variability of each measure as a function of TE between SFP voxels. Additionally, the much noisier data at longer TEs could also have contributed to these differences. Yet, for echo times ≥ 75 ms we observed a decrease in RD and an increase in FA, which agree with observations made by Qin et al. [58] and Lin et al. [59], and similar to the latter we saw no significant changes in AD.

From the same data compartmental transverse relaxation rates were previously estimated [21], and faster extra-axonal signal decay was observed, which is in correspondence with previous findings [56, 57, 60, 61].

4.2. Head-orientation dependence of DT measures

Orientational anisotropy of DT measures observed in vivo and in silico.

We estimated non-zero magnitude of orientation anisotropy in all DTI measures with both methods: pooled SFP voxels, and tract-segment-wise comparison between default and tilted head orientations. Under the assumption of $\sin^4\theta$ -behaviour, the

correspondence in estimated magnitude of anisotropy between the two methods was higher at shorter echo times of 54 ms and 75 ms, the accuracy at longer echo times was potentially compromised by decreased SNR. Similarly, the contribution of anisotropy effects to the variance of DTI measures decreased with increasing echo time. Comparing the spline with the $\sin^4\theta$ -representation in the pooled results, the absolute values of B obtained using spline fitting were subtly higher than those estimated using the $\sin^4\theta$ -approximation, but overall followed the same trend as a function of TE.

The *in vivo* RD and MD estimates as a function of θ followed trends also seen in the analytical simulations, i.e. positive B for AD and FA and negative B for RD. However, also opposite signs for B were observed in the noisy simulations, e.g. in AD. This could not merely be caused by $D_{e,\parallel} > D_{i,\parallel}$ (the opposite was simulated), but it is hypothesised that this could be attributed to the complexity of tissue (e.g. dispersion, a distribution of diffusivities and T_2 within and across voxels in the *in vivo* results, and other origins of orientation dependence) and different levels of noise, amongst others. One can also observe that the estimated B of AD decreased as function of TE *in vivo* in contrast to the increase in the toy-example.

Origin of anisotropic effects of DTI in WM. The simulations considered the

effect of T_2 -weighting and different T_2 -anisotropy behaviour in the intra- and extra-axonal space on DT measures, assuming a dominant role for myelin susceptibility effects in the extra-axonal space. However, the origin of the orientation dependence may be more complex. In *in vivo* data both the $\sin^4\theta$ behaviour and a more general spline representation were used to investigate the θ -dependence, indeed resulting in a similar estimated contribution of orientation-dependence to the variance of DT measures in the pooled analysis and similar magnitudes of anisotropy. This similarity partially supported the assumption made in simulations, i.e., that the difference in $R_2(\theta)$ -dependence between the intra- and extra-axonal signals (i.e. $\sin^4\theta$ -dependence in the extra-axonal space) is a major contributor to the orientational anisotropy. Yet the behaviour of the spline curves deviates from the typical $\sin^4\theta$ -shape which indeed suggests that the nature of anisotropy must be more complex.

The hypothesis that self-induced gradients arising from local variations in magnetic susceptibility could be an additional source of variation in apparent diffusion coefficients has been proposed by several works [26, 30]. Trudeau et al. [30] measured diffusivity values at 4.7T in excised porcine spinal cords at room temperature, with diffusion gradients applied parallel and perpendicular to the primary fibre orientation. By reorienting the sample relative to the main magnetic

field direction, they were able to manipulate the distribution of local magnetic susceptibility. Beaulieu and Allen [26] performed similar experiments at 2.35T on excised nerve fibres from garfish and frog. Both studies reported no detectable impact of local gradients on diffusivity values in these samples, and neither attributed the observed [26] orientation dependence w.r.t. \vec{B}_0 to the effects of local gradients. Upon closer inspection of [30, FIG. 3], a trend may be apparent with regards to fibre orientation w.r.t. \vec{B}_0 . Although the distributions of D_{\parallel} - or D_{\perp} -values overlap when measured at either sample orientation, the average values for D_{\parallel} seem lower and the average values for D_{\perp} seem higher when the primary fibre orientation is along \vec{B}_0 . Beaulieu and Allen [26] solidified the apparent trend for the dependence of D_{\parallel} -values on primary fibre orientation w.r.t. \vec{B}_0 , by reporting 15% lower values measured when fibres were along the magnetic field. Similarly, in our in vivo data axial diffusivities were higher for fibres across \vec{B}_0 compared to fibres along \vec{B}_0 , while radial diffusivities followed the opposite trend. Knight et al. [15] have previously simulated the effects of mesoscopic magnetic field inhomogeneities near a hollow cylinder on T_2 and also reported head-orientation dependence of MD and FA values. They considered cross-terms between local gradients and encoding gradients to be negligible. Wang et al.[62] have rotated an extracted mouse brain w.r.t. the main magnetic field and evaluated MD and FA for seven major brain

regions, one of which was white matter. They did not observe any significant variations across orientations of MD/FA in WM, however they did not break down WM into sub-ROIs of similar fibre orientation, potentially averaging away effects due to re-orientation. Bartels et al. [63] have recently studied MD, AD and RD as function of fibre orientation w.r.t. \vec{B}_0 . They reported MD to behave in correspondence with simulations by Knight et al. [15], but AD/RD obtained from their data are respectively minimal/maximal around the magic angle, suggesting a different origin of anisotropy. Interestingly, our data showed similar trends (cf., spline curves or piecewise average in SI). RD also showed a local maximum near the magic angle. The AD-curves appeared monotonous but still an increase in gradient around the same angle was evident. Additionally, a local minimum was apparent in the FA-curves. Pang [64, 65] also suggests an important role for magic angle effects.

Studies which investigate the \vec{B}_0 -related anisotropic effects in DTI are limited in number. Yet, the anisotropic effects in DTI measures from WM observed here are coherent with those seen in previous works investigating $R_2^{(*)}$ -anisotropy, though comparatively less pronounced. The majority of studies cover anisotropic effects of the WM signal evolution from the multi-echo gradient-recalled-echo (mGRE) sequence [1–12]: thanks to its sensitivity to B_0 -inhomogeneities it provides strong contrast in regions composed of tissues with different magnetic susceptibilities

(myelinated WM fibres, in this particular case). Although most dMRI sequences are spin-echo-based, in which the B_0 -effects are refocused, some magnetic susceptibility effects may shine through. On one hand, incoherent molecular motion happening between the excitation pulse and the spin-echo combined with local B_0 -inhomogeneities induced by the myelin sheath may lead to residual non-fully-refocused phases, on the other hand, echo-planar readout has some unavoidable R_2^* -weighting during the acquisition window. That said, the centre of the k -space is closer to the centre spin-echo, and is therefore less affected; additionally, lower-resolution data are expected to suffer less from this effect. Indeed, Gil et al. [14] reported $\sin^4\theta$ -dependence of macroscopic R_2 -values on fibre orientation θ to \vec{B}_0 .

Another candidate for the orientational dependence of R_2 is the aforementioned magic angle effect (or dipole-dipole interactions) with the characteristic $(3\cos^2\theta - 1)^2$ -behaviour. So far those were not considered the primary source of WM R_2 -anisotropy in adults in vivo and postmortem brain, but also not excluded as a potential contributor [6, 11, 66]. Interestingly, Bartels et al. [20] studied R_2 orientation dependence in the newborn brain having low myelination and observed very different behaviour from the adult brain, suggesting a primary role for residual dipolar coupling. In the absence of myelin,

neurofilaments and microtubules of the axonal cytoskeleton are aligned with the axon were hypothesised to contribute to orientation-dependence. Similar observations were made on our data separating the intra- and extra-axonal relaxation rates [21]: $R_2(\theta) \sim (3\cos^2\theta - 1)^2$ fitted the intra-axonal data best.

Summarising, compartmental $R_2^{(*)}$ -values have been reported to depend on orientation differentially [7, 9, 21, 67], which could intrinsically lead to DT-dependence on fibre orientation w.r.t. \vec{B}_0 , regardless of the underlying microscopic mechanisms.

4.3. Limitations and future work

Anatomical correspondence. The pooled analysis considers all single fibre population voxels throughout the WM together to estimate a single magnitude of orientation dependence, however the simulations reveal that micro-anatomical differences (e.g., signal fractions, myelin sheath thickness, fibre density and other potential contributors to compartmental T_2 -differences) can lead to different orientation dependence. The tractometry analysis aims to address this to a certain extent by pooling voxels more locally, but with two head orientations as used in this study it remains challenging to estimate local differences in orientation dependence.

More head orientations and a boost in SNR could help to further investigate this. Here, more efficient acquisition-schemes, such as ZEBRA [68], would be beneficial to enable reasonable acquisition times. Moreover, anatomical correspondence could be further achieved by co-registering the data from the two head orientations in future work. To accomplish this, it is essential to employ a reliable registration method that can effectively handle the residual nonlinear effects. Furthermore, by pooling the data from all subjects' SFP WM voxels we were able to compensate for low number of subjects. With more subjects one could investigate the anisotropy w.r.t. B_0 of individual tracts and consequently provide additional anatomical information.

Gradient nonlinearities. Another limitation potentially arises from nonlinearities of gradient fields. With the rotation of the tiltable coil the head is positioned further from the iso-centre, where gradient nonlinearities have a larger effect. This in turn influences the effective B -matrix, and could introduce additional variability between the non-tilted and tilted orientation. In addition to effects reported as a result of the effective B -matrix not being taken into account [69–71], if gradient nonlinearities cause the effective b -value to be higher than the imposed value, kurtosis effects may start to play a more prominent role and bias DT estimates. In the current work we take into account the effective B -matrices, and to

further minimise this potential confound we analysed a subset of the data at $TE = 54$ ms for which a lower b -value of 1050 s/mm² was available (Figure 1A). Supplementary Figure S4 shows a comparison of the pooled- and tractometry-analyses with maximum b -value of 1500 s/mm² and 1050 s/mm². The observation of orientation dependence remained unchanged, with larger estimated absolute magnitude of anisotropy at the lower b -value for AD, RD, and FA in both analyses and also MD in the tractometry analysis.

We also considered the effect of gradient non-linearities in the estimation of the fibre direction. In this work, the first eigenvector of the DT was used, but this can be done in alternative ways and with different estimation techniques, e.g. spherical deconvolution to obtain the fODF. The reason this work opted for the current approach is that spherical deconvolution approaches typically do not take into account gradient nonlinearities [70]. The DT estimation used in this manuscript does take this into account and the estimates of the maps and fibre direction come from the same DT estimate.

Crossing fibres. This scope of this work is limited to single fibre population voxels. Previous work has characterised T_2 per fibre population in crossing fibre voxels, for example [72]. In the current work, based on [21], we have simulated a

distribution of orientation-dispersed compartments according to a Watson distribution, where each sub-compartment (e.g. each extra-axonal zeppelin) can separately exhibit R_2 -orientation dependence. This could be straightforwardly adapted to model crossing fibres, but the bundles will have to have the same relaxation properties. A recently presented abstract described estimation of such a model for multi-echo gradient-echo sequences [73].

SNR. Finally, the SNR distribution in WM can change with head-reorientation. While the tiltable coil minimises differences in the coil-to-brain distance across different head orientations, SNR may still be affected due to e.g. change in the reception efficiency of the tiltable coil as the axis of the coil is rotated away from \vec{B}_0 , gradient non-uniformities, or B_0 shim. Previous work [21] showed that the temporal SNR (tSNR) distribution in WM globally overlapped between tilted and default orientation, and Supplementary Figure S5 further investigates this per tract-segment from the tractometry pipeline. Overall the estimated tSNR of the same location in tilted vs default orientation is distributed along the line $y = x$, but a global fit through tSNR measurements from all locations implies that tSNR values in the tilted position could be up to 15% lower than in the default orientation. Preliminary experiments in a phantom with the body coils for signal reception suggest that the impact of B_0 shim and gradient non-uniformities may be greater

than the impact of receive coil efficiency (results not shown). While we have attempted to correct for noise bias – which can significantly impact DTI estimates [74] – denoising strategies could further reduce the impact of noise-differences especially at longer TE.

5. Conclusion

DT measures may vary up to 20% as a function of WM fibre orientation w.r.t. \vec{B}_0 in the scenarios investigated. Fibre orientation can be responsible for up to 7% variance in diffusion tensor measures across single fibre populations of the whole brain white matter. While potentially containing useful information on e.g. myelination, the orientation dependence of DTI w.r.t. \vec{B}_0 can be an additional source of variance camouflaging the effect-of-interest in clinical research studies, particularly when the effect size is small and it is difficult to control for fibre orientation w.r.t. \vec{B}_0 (e.g. fetal or neonatal imaging, or when the trajectories of fibres change due to e.g. space occupying lesions).

Acknowledgements

For the purpose of open access, the author has applied a CC BY public

copyright licence to any Author Accepted Manuscript version arising from this submission. CMWT is supported by the Wellcome Trust [215944/Z/19/Z] and a Veni grant (17331) from the Dutch Research Council (NWO). DKJ, CMWT, and EK were all supported by a Wellcome Trust Investigator Award (096646/Z/11/Z) and DKJ and EK were supported by a Wellcome Strategic Award (104943/Z/14/Z).

The data were acquired at the UK National Facility for In Vivo MR Imaging of Human Tissue Microstructure funded by the EPSRC (grant EP/M029778/1), and The Wolfson Foundation.

We would like to thank Siemens Healthineers, and particularly Fabrizio Fasano, Peter Gall, and Matschl Volker, for the provision of the tiltable RF-coil used in this work. We would also like to thank John Evans, Greg Parker and Umesh Rudrapatna for technical support, Maxime Chamberland for the tractometry analysis in the original publication on compartmental T_2 -anisotropy, and Stefano Zappalà for helpful discussions.

Data Availability Statement

Data available on request due to privacy/ethical restrictions.

Author Contributions

EK: Conceptualization; Formal analysis; Investigation; Methodology; Software; Validation; Visualization; Writing – original draft; Writing – review & editing.

DK: Funding acquisition; Resources; Writing – review & editing.

CMWT: Conceptualization; Formal analysis; Investigation; Methodology; Project administration; Software; Supervision; Validation; Writing – original draft; Writing – review & editing

Declaration of Competing Interests

No conflict of interest to disclose.

References

[1] B. Bender and U. Klose. The in vivo influence of white matter fiber

orientation towards B_0 on T_2^* in the human brain. *NMR in Biomedicine*, 23(9):1071–1076, nov 2010. ISSN 09523480. doi: 10.1002/nbm.1534.

[2] Andrea Cherubini, Patrice Péran, Gisela Elisabeth Hagberg, Ambra Erika Varsi, Giacomo Luccichenti, Carlo Caltagirone, Umberto Sabatini, and Gianfranco Spalletta. Characterization of white matter fiber bundles with T_2^* relaxometry and diffusion tensor imaging. *Magnetic Resonance in Medicine*, 61(5):1066–1072, 2009. doi: 10.1002/mrm.21978. URL <https://onlinelibrary.wiley.com/doi/abs/10.1002/mrm.21978>.

[3] Christian Denk, Eneidino Hernandez Torres, Alex MacKay, and Alexander Rauscher. The influence of white matter fibre orientation on MR signal phase and decay. *NMR in Biomedicine*, 24(3):246–252, 2011. doi: 10.1002/nbm.1581.

[4] C Wiggins, V Gudmundsdottir, D Le Bihan, V Lebon, and M Chaumeil. Orientation Dependence of White Matter T_2^* Contrast at 7 T : A Direct Demonstration. In *Proceedings 16th Scientific Meeting, International Society for Magnetic Resonance in Medicine, Toronto, 2008*.

[5] Jongho Lee, Karin Shmueli, Masaki Fukunaga, Peter van Gelderen, Hellmut Merkle, Afonso C Silva, and Jeff H Duyn. Sensitivity of MRI resonance frequency to the orientation of brain tissue microstructure. *Proceedings of the National Academy of Sciences*, 107(11):5130–5135, mar 2010. ISSN 0027-8424. doi: 10.1073/pnas.0910222107.

[6] Jongho Lee, Peter van Gelderen, Li-Wei Kuo, Hellmut Merkle, Afonso C. Silva, and Jeff H. Duyn. T_2^* -based fiber orientation mapping. *NeuroImage*, 57(1):225 – 234, 2011. ISSN 1053-8119. doi: 10.1016/j.neuroimage.2011.04.026.

[7] Samuel Wharton and Richard Bowtell. Fiber orientation-dependent white matter contrast in gradient echo MRI. *Proceedings of the National Academy of Sciences of the United States of America*, 109(45):18559–18564, nov 2012. ISSN 00278424. doi: 10.1073/pnas.1211075109.

[8] Pascal Sati, Afonso C. Silva, Peter van Gelderen, Maria I. Gaitan, Jillian E. Wohler, Steven Jacobson, Jeff H. Duyn, and Daniel S. Reich. In vivo quantification of T_2^* anisotropy in white matter fibers in marmoset monkeys. *NeuroImage*, 59(2):979 – 985, 2012. ISSN 1053-8119. doi: 10.1016/j.neuroimage.2011.08.064. URL

<http://www.sciencedirect.com/science/article/pii/S1053811911009815>.

[9] Pascal Sati, Peter van Gelderen, Afonso C. Silva, Daniel S. Reich, Hellmut Merkle, Jacco A. De Zwart, and Jeff H. Duyn. Micro-compartment specific T_2^* relaxation in the brain. *NeuroImage*, 77:268–278, aug 2013. ISSN 10538119. doi: 10.1016/j.neuroimage.2013.03.005.

[10] Samuel Wharton and Richard Bowtell. Gradient echo based fiber orientation mapping using R_2^* and frequency difference measurements. *NeuroImage*, 83:1011 – 1023, 2013. ISSN 1053-8119. doi: 10.1016/j.neuroimage.2013.07.054.

[11] Se-Hong Oh, Young-Bo Kim, Zang-Hee Cho, and Jongho Lee. Origin of B_0 orientation dependent $R_2^*(= 1/T_2^*)$ in white matter. *NeuroImage*, 73:71 – 79, 2013. ISSN 1053-8119. doi: doi.org/10.1016/j.neuroimage.2013.01.051. URL <http://www.sciencedirect.com/science/article/pii/S1053811913000980>.

[12] David A. Rudko, L. Martyn Klassen, Sonali N. De Chickera, Joseph S.

Gati, Gregory A. Dekaban, and Ravi S. Menon. Origins of R_2^* orientation dependence in gray and white matter. *Proceedings of the National Academy of Sciences of the United States of America*, 111(1), 2014. ISSN 00278424. doi: 10.1073/pnas.1306516111.

[13] Michael J. Knight, Bryony Wood, Elizabeth Couthard, and Risto Kauppinen. Anisotropy of spin-echo T_2 relaxation by magnetic resonance imaging in the human brain in vivo. *Biomedical Spectroscopy and Imaging*, 4(3):299–310, jun 2015. ISSN 22128808. doi: 10.3233/BSI-150114. URL <http://www.medra.org/servlet/aliasResolver?alias=iospress&doi=10.3233/BSI-150114>.

[14] Rita Gil, Diana Khabipova, Marcel Zwiers, Tom Hilbert, Tobias Kober, and José P. Marques. An in vivo study of the orientation-dependent and independent components of transverse relaxation rates in white matter. *NMR in Biomedicine*, 29(12):1780–1790, dec 2016. ISSN 10991492. doi: 10.1002/nbm.3616.

[15] Michael J. Knight, Serena Dillon, Lina Jarutyte, and Risto A. Kauppinen. Magnetic Resonance Relaxation Anisotropy: Physical Principles and Uses in Microstructure Imaging. *Biophysical Journal*, 112(7):1517–1528, apr 2017. ISSN

15420086. doi: 10.1016/j.bpj.2017.02.026.

[16] André Pampel, Dirk K. Müller, Alfred Anwander, Henrik Marschner, and Harald E. Möller. Orientation dependence of magnetization transfer parameters in human white matter. *NeuroImage*, 114:136 – 146, 2015. ISSN 1053-8119. doi: <https://doi.org/10.1016/j.neuroimage.2015.03.068>. URL <http://www.sciencedirect.com/science/article/pii/S1053811915002645>.

[17] Felix Schyboll, Uwe Jaekel, Bernd Weber, and Heiko Neeb. The impact of fibre orientation on T_1 -relaxation and apparent tissue water content in white matter. *Magnetic Resonance Materials in Physics, Biology and Medicine*, 2018. ISSN 13528661. doi: 10.1007/s10334-018-0678-8.

[18] Felix Schyboll, Uwe Jaekel, Francesco Petruccione, and Heiko Neeb. Fibre-orientation dependent R_1 ($= 1/T_1$) relaxation in the brain: The role of susceptibility induced spin-lattice relaxation in the myelin water compartment. *Journal of Magnetic Resonance*, 300:135 – 141, 2019. ISSN 1090-7807. doi: <https://doi.org/10.1016/j.jmr.2019.01.013>. URL <http://www.sciencedirect.com/science/article/pii/S1090780719300135>.

[80719300138.](#)

[19] Michael J. Knight, Robin A. Damion, and Risto A. Kauppinen. Observation of angular dependence of T_1 in the human white matter at 3T. *Biomedical Spectroscopy and Imaging*, 2018. ISSN 22128794. doi: 10.3233/bsi-180183.

[20] Lara M. Bartels, Jonathan Doucette, Christoph Birkl, Yuting Zhang, Alexander M. Weber, and Alexander Rauscher. Orientation dependence of r_2 relaxation in the newborn brain. *NeuroImage*, 264:119702, 2022. ISSN 1053-8119. doi: 10.1016/j.neuroimage.2022.119702. URL <https://doi.org/10.1016/j.neuroimage.2022.119702>.

[21] Chantal M.W. Tax, Elena Kleban, Maxime Chamberland, Muhamed Barakovć, Umesh Rudrapatna, and Derek K. Jones. Measuring compartmental T_2 -orientational dependence in human brain white matter using a tiltable RF coil and diffusion- T_2 correlation MRI. *NeuroImage*, 236:117967, 2021. ISSN 1053-8119. doi: 10.1016/j.neuroimage.2021.117967.

[22] Emilie T. McKinnon and Jens H. Jensen. Measuring intra-axonal T_2 in

white matter with direction-averaged diffusion MRI. *Magnetic Resonance in Medicine*, 81(5):2985–2994, 2019. ISSN 07403194. doi: 10.1002/mrm.27617.

[23] P.J. Basser, J. Mattiello, and D. Lebihan. Estimation of the Effective Self-Diffusion Tensor from the NMR Spin Echo, 1994. ISSN 10641866. URL <https://doi.org/10.1006/jmrb.1994.1037>.

[24] Jianhui Zhong, Richard P Kennan, and John C Gore. Effects of susceptibility variations on NMR measurements of diffusion. *Journal of Magnetic Resonance (1969)*, 95(2):267–280, November 1991. ISSN 0022-2364. URL <https://doi.org/10.1006/jmre.1999.1872>.

[25] Jianhui Zhong and John C. Gore. Studies of restricted diffusion in heterogeneous media containing variations in susceptibility. *Magnetic Resonance in Medicine*, 19(2):276–284, 1991. ISSN 1522-2594. URL <https://doi.org/10.1002/mrm.1910190215>.

[26] Christian Beaulieu and Peter S. Allen. An in vitro evaluation of the effects of local magnetic-susceptibility-induced gradients on anisotropic water diffusion in nerve. *Magnetic Resonance in Medicine*, 36(1):39–44, 1996. URL

<https://doi.org/10.1002/mrm.1910360108>.

[27] C. A. Clark, G. J. Barker, and P. S. Tofts. An in Vivo Evaluation of the Effects of Local Magnetic Susceptibility-Induced Gradients on Water Diffusion Measurements in Human Brain. *Journal of Magnetic Resonance*, 141(1):52–61, November 1999. ISSN 1090-7807. URL

<https://doi.org/10.1006/jmre.1999.1872>.

[28] Mark D. Does, Jianhui Zhong, and John C. Gore. In vivo measurement of ADC change due to intravascular susceptibility variation. *Magnetic Resonance in Medicine*, 41(2):236–240, 1999. ISSN 1522-2594. URL

[https://doi.org/10.1002/\(SICI\)1522-2594\(199902\)41:2<236::AID-MRM4>3.0.CO;2-3](https://doi.org/10.1002/(SICI)1522-2594(199902)41:2<236::AID-MRM4>3.0.CO;2-3).

[29] Dmitry S. Novikov, Marco Reisert, and Valerij G. Kiselev. Effects of mesoscopic susceptibility and transverse relaxation on diffusion nmr. *Journal of Magnetic Resonance*, 293:134–144, 2018. ISSN 1090-7807. URL

<https://doi.org/10.1016/j.jmr.2018.06.007>.

[30] J.D. Trudeau, W.T. Dixon, and J. Hawkins. The effect of inhomogeneous

sample susceptibility on measured diffusion anisotropy using nmr imaging. *Journal of Magnetic Resonance, Series B*, 108(1):22–30, 1995. ISSN 1064-1866. doi:

<https://doi.org/10.1006/jmrb.1995.1098>. URL

<https://doi.org/10.1006/jmrb.1995.1098>.

[31] Dmitry S. Novikov, Els Fieremans, Sune N. Jespersen, and Valerij G. Kiselev. Quantifying brain microstructure with diffusion MRI: Theory and parameter estimation. *NMR in Biomedicine*, 32(4):e3998, 2019. URL

<https://doi.org/10.1002/nbm.3998>.

[32] Yaniv Assaf and Peter J. Basser. Composite hindered and restricted model of diffusion (charmed) mr imaging of the human brain. *NeuroImage*, 27(1):48–58, 2005. ISSN 1053-8119. URL

<https://doi.org/10.1016/j.neuroimage.2005.03.042>.

[33] Christopher D. Kroenke, Joseph J.H. Ackerman, and Dmitriy A. Yablonskiy. On the nature of the NAA diffusion attenuated MR signal in the central nervous system. *Magnetic Resonance in Medicine*, 52(5):1052–1059, nov 2004.

ISSN 0740-3194. doi: 10.1002/mrm.20260. URL

<http://doi.wiley.com/10.1002/mrm.20260>.

[34] Sune N. Jespersen, Christopher D. Kroenke, Leif Østergaard, Joseph J.H. Ackerman, and Dmitriy A. Yablonskiy. Modeling dendrite density from magnetic resonance diffusion measurements. *NeuroImage*, 34(4):1473–1486, feb 2007. ISSN 1053-8119. URL <https://doi.org/10.1016/J.NEUROIMAGE.2006.10.037>.

[35] Jens H. Jensen, Joseph A. Helpern, Anita Ramani, Hanzhang Lu, and Kyle Kaczynski. Diffusional kurtosis imaging: The quantification of non-gaussian water diffusion by means of magnetic resonance imaging. *Magnetic Resonance in Medicine*, 53(6):1432–1440, 2005. URL <https://doi.org/10.1002/mrm.20508>.

[36] H. Akaike. A new look at the statistical model identification. *IEEE Transactions on Automatic Control*, 19(6):716–723, 1974. doi: 10.1109/TAC.1974.1100705.

[37] Kenneth P. Burnham and David R. Anderson. Multimodel inference: Understanding aic and bic in model selection. *Sociological Methods & Research*, 33(2):261–304, 2004. doi: 10.1177/0049124104268644. URL

<https://doi.org/10.1177/0049124104268644>.

[38] Todd W. Arnold. Uninformative parameters and model selection using akaike's information criterion. *The Journal of Wildlife Management*, 74(6):1175–1178, 2010. doi: 10.1111/j.1937-2817.2010.tb01236.x . URL <https://wildlife.onlinelibrary.wiley.com/doi/abs/10.1111/j.1937-2817.2010.tb01236.x>.

[39] Viljami Sairanen, Alexander Leemans, and Chantal MW Tax. Fast and accurate Slicewise OutLier Detection (SOLID) with informed model estimation for diffusion MRI data. *NeuroImage*, 181:331–346, 2018. doi: 10.1016/J.NEUROIMAGE.2018.07.003.

[40] Elias Kellner, Bibek Dhital, Valerij G. Kiselev, and Marco Reisert. Gibbs-ringing artifact removal based on local subvoxel-shifts. *Magnetic Resonance in Medicine*, 76(5):1574–1581, 2016. doi: 10.1002/mrm.26054.

[41] Jesper L.R. Andersson, Stefan Skare, and John Ashburner. How to correct susceptibility distortions in spin-echo echo-planar images: application to diffusion tensor imaging. *NeuroImage*, 20(2):870–888, 2003. doi:

10.1016/S1053-8119(03)00336-7.

[42] Jesper L.R. Andersson and Stamatios N. Sotiropoulos. An integrated approach to correction for off-resonance effects and subject movement in diffusion MR imaging. *NeuroImage*, 125:1063–1078, 2016. doi: 10.1016/j.neuroimage.2015.10.019.

[43] Matthew F. Glasser, Stamatios N. Sotiropoulos, J. Anthony Wilson, Timothy S. Coalson, Bruce Fischl, Jesper L. Andersson, Junqian Xu, Saad Jbabdi, Matthew Webster, Jonathan R. Polimeni, David C. Van Essen, and Mark Jenkinson. The minimal preprocessing pipelines for the Human Connectome Project. *NeuroImage*, 80:105–124, 2013. doi: 10.1016/J.NEUROIMAGE.2013.04.127.

[44] Cheng Guan Koay, Evren Özarlan, and Carlo Pierpaoli. Probabilistic Identification and Estimation of Noise (PIESNO): A self-consistent approach and its applications in MRI. *Journal of Magnetic Resonance*, 199(1):94–103, 2009. doi: 10.1016/J.JMR.2009.03.005.

[45] Cheng Guan Koay, Evren Ozarlan, and Peter J Basser. A signal transformational framework for breaking the noise floor and its applications in MRI.

Journal of magnetic resonance (San Diego, Calif. : 1997), 197(2):108–19, 2009.
doi: 10.1016/j.jmr.2008.11.015.

[46] Samuel St-Jean, Pierrick Coupé, and Maxime Descoteaux. Non Local Spatial and Angular Matching: Enabling higher spatial resolution diffusion MRI datasets through adaptive denoising. *Medical Image Analysis*, 32:115–130, 2016.
doi: 10.1016/J.MEDIA.2016.02.010.

[47] Samuel St-Jean, Alberto De Luca, Chantal M.W. Tax, Max A. Viergever, and Alexander Leemans. Automated characterization of noise distributions in diffusion MRI data. *Medical Image Analysis*, page 101758, 2020. doi:
10.1016/j.media.2020.101758.

[48] Umesh Rudrapatna, Greg D. Parker, Jamie Roberts, and Derek K. Jones. A comparative study of gradient nonlinearity correction strategies for processing diffusion data obtained with ultra-strong gradient MRI scanners. *Magnetic Resonance in Medicine*, 85(2):1104–1113, 2021. doi:
<https://doi.org/10.1002/mrm.28464>. URL
<https://onlinelibrary.wiley.com/doi/abs/10.1002/mrm.28464>
[64](#).

[49] J-Donald Tournier, Fernando Calamante, and Alan Connelly. Robust determination of the fibre orientation distribution in diffusion MRI: Non-negativity constrained super-resolved spherical deconvolution. *NeuroImage*, 35(4):1459–1472, 2007. doi: 10.1016/j.neuroimage.2007.02.016.

[50] Maxime Descoteaux, Rachid Deriche, Thomas R Knosche, and Alfred Anwander. Deterministic and probabilistic tractography based on complex fibre orientation distributions. *IEEE transactions on medical imaging*, 28(2):269–286, 2008.

[51] Ben Jeurissen, Jacques Donald Tournier, Thijs Dhollander, Alan Connelly, and Jan Sijbers. Multi-tissue constrained spherical deconvolution for improved analysis of multi-shell diffusion MRI data. *NeuroImage*, 103:411–426, 2014. doi: 10.1016/j.neuroimage.2014.07.061.

[52] Chantal MW Tax, Ben Jeurissen, S.B. Vos, M.A. Viergever, and A. Leemans. Recursive calibration of the fiber response function for spherical deconvolution of diffusion MRI data. *NeuroImage*, 86, 2014. doi: 10.1016/j.neuroimage.2013.07.067.

[53] Marco Reisert, Elias Kellner, Bibek Dhital, Jürgen Hennig, and Valerij G. Kiselev. Disentangling micro from mesostructure by diffusion MRI: A Bayesian approach. *NeuroImage*, 147:964–975, feb 2017. ISSN 1053-8119. doi: 10.1016/J.NEUROIMAGE.2016.09.058. URL <https://www.sciencedirect.com/science/article/pii/S1053811916305353?via%3Dihub>.

[54] Dmitry S. Novikov, Jelle Veraart, Ileana O. Jelescu, and Els Fieremans. Rotationally-invariant mapping of scalar and orientational metrics of neuronal microstructure with diffusion MRI. *NeuroImage*, 174:518–538, jul 2018. ISSN 1053-8119. doi: 10.1016/J.NEUROIMAGE.2018.03.006. URL <https://www.sciencedirect.com/science/article/pii/S1053811918301915?via%3Dihub>.

[55] Jakob Wasserthal, Peter Neher, and Klaus H. Maier-Hein. TractSeg - Fast and accurate white matter tract segmentation. *NeuroImage*, 183:239–253, 2018. ISSN 10959572. doi: 10.1016/j.neuroimage.2018.07.070.

[56] Mark D. Does and John C. Gore. Compartmental study of diffusion and

relaxation measured in vivo in normal and ischemic rat brain and trigeminal nerve.

Magnetic Resonance in Medicine, 43(6):837–844, 2000. doi:

10.1002/1522-2594(200006)43:6<837::AID-MRM9>3.0.CO;2-O.

[57] Yaniv Assaf and Yoram Cohen. Assignment of the water slow-diffusing component in the central nervous system using q -space diffusion MRS:

Implications for fiber tract imaging. *Magnetic Resonance in Medicine*,

43(2):191–199, 2000. doi:

10.1002/(SICI)1522-2594(200002)43:2<191::AID-MRM5>3.0.CO;2-B.

[58] Wen Qin, Chun Shui Yu, Fan Zhang, Xiang Ying Du, Heng Jiang, Yu Xia Yan, and Kun Cheng Li. Effects of echo time on diffusion quantification of

brain white matter at 1.5t and 3.0t. *Magnetic Resonance in Medicine*,

61(4):755–760, 2009. doi: 10.1002/mrm.21920. URL

[https://onlinelibrary.wiley.com/doi/abs/10.1002/mrm.219](https://onlinelibrary.wiley.com/doi/abs/10.1002/mrm.21920)

[20](https://onlinelibrary.wiley.com/doi/abs/10.1002/mrm.21920).

[59] Mu Lin, Hongjian He, Qiqi Tong, Qiuping Ding, Xu Yan, Thorsten Feiweier, and Jianhui Zhong. Effect of myelin water exchange on DTI-derived

parameters in diffusion MRI: Elucidation of TE dependence. *Magnetic Resonance*

in Medicine, 79(3):1650–1660, 2018. doi: 10.1002/mrm.26812.

[60] Sharon Peled, David G. Cory, Stephen A. Raymond, Daniel A. Kirschner, and Ferenc A. Jolesz. Water diffusion, T_2 , and compartmentation in frog sciatic nerve. *Magnetic Resonance in Medicine*, 42(5):911–918, nov 1999. ISSN 0740-3194. doi: 10.1002/(SICI)1522-2594(199911)42:5<911::AID-MRM11>3.0.CO;2-J. URL <http://doi.wiley.com/10.1002/%28SICI%291522-2594%28199911%2942%3A5%3C911%3A%3AAID-MRM11%3E3.0.CO%3B2-J>.

[61] Jelle Veraart, Dmitry S. Novikov, and Els Fieremans. TE dependent Diffusion Imaging (TEdDI) distinguishes between compartmental T_2 relaxation times. *NeuroImage*, 182:360–369, nov 2018. ISSN 1053-8119. doi: 10.1016/J.NEUROIMAGE.2017.09.030. URL <https://www.sciencedirect.com/science/article/pii/S1053811917307784?via%3Dihub>.

[62] Nian Wang, Qiuting Wen, Surendra Maharjan, Anthony J. Mirando, Yi Qi, Matthew J. Hilton, and Charles E. Spritzer. Magic angle effect on diffusion tensor imaging in ligament and brain. *Magnetic Resonance Imaging*, 92:243–250,

2022. ISSN 0730-725X. doi: 10.1016/j.mri.2022.06.008. URL

<https://doi.org/10.1016/j.mri.2022.06.008>.

[63] Lara Bartels, Jonathan Doucette, Christoph Birkl, Alexander M. Weber, and Alexander Rauscher. Diffusion metrics in human white matter depend on fibre orientation. In *ISMRM*, page 2456, 2022. URL

<https://cds.ismrm.org/protected/22MPresentations/abstracts/2456.html>.

[64] Yuxi Pang. Is diffusion tensor principal diffusivity aligned with axon fibre in the human brain white matter? In *ISMRM*, page 0648, 2022. URL

<https://cds.ismrm.org/protected/22MPresentations/abstracts/0648.html>.

[65] Yuxi Pang. Orientation dependent proton transverse relaxation in the human brain white matter: The magic angle effect on a cylindrical helix. *Magnetic Resonance Imaging*, 100:73–83, 2023. URL

<https://doi.org/10.1016/j.mri.2023.03.010>.

[60] Christoph Birkl, Jonathan Doucette, Michael Fan, Enedino

Hernández-Torres, and Alexander Rauscher. Myelin water imaging depends on white matter fiber orientation in the human brain. *Magnetic Resonance in Medicine*, n/a(n/a), 2020. doi: 10.1002/mrm.28543. URL <https://onlinelibrary.wiley.com/doi/abs/10.1002/mrm.28543>.

[67] Elena Kleban, Chantal M.W. Tax, Umesh S. Rudrapatna, Derek K. Jones, and Richard Bowtell. Strong diffusion gradients allow the separation of intra- and extra-axonal gradient-echo signals in the human brain. *NeuroImage*, 217:116793, 2020. ISSN 1053-8119. doi: <https://doi.org/10.1016/j.neuroimage.2020.116793>. URL <http://www.sciencedirect.com/science/article/pii/S1053811920302809>.

[68] Jana Hutter, Paddy J. Slator, Daan Christiaens, Rui Pedro A. G. Teixeira, Thomas Roberts, Laurence Jackson, Anthony N. Price, Shaihan Malik, and Joseph V. Hajnal. Integrated and efficient diffusion-relaxometry using ZEBRA. *Scientific Reports*, 8(1):15138, dec 2018. ISSN 2045-2322. doi: 10.1038/s41598-018-33463-2. URL <http://www.nature.com/articles/s41598-018-33463-2>.

[69] R. Bammer, M. Markl, A. Barnett, B. Acar, M.T. Alley, N.J. Pelc, G.H. Glover, and M.E. Moseley. Analysis and generalized correction of the effect of spatial gradient field distortions in diffusion-weighted imaging. *Magnetic Resonance in Medicine*, 50(3):560–569, sep 2003. ISSN 0740-3194. doi: 10.1002/mrm.10545. URL <http://doi.wiley.com/10.1002/mrm.10545>.

[70] Fenghua Guo, Alberto De Luca, Greg Parker, Derek K Jones, Max A Viergever, Alexander Leemans, and Chantal MW Tax. The effect of gradient nonlinearities on fiber orientation estimates from spherical deconvolution of diffusion magnetic resonance imaging data. *Human Brain Mapping*, 42(2):367–383, 2020. doi: 10.1002/hbm.25228. URL <https://onlinelibrary.wiley.com/doi/abs/10.1002/hbm.25228>.

[71] Hamed Y. Mesri, Szabolcs David, Max A. Viergever, and Alexander Leemans. The adverse effect of gradient nonlinearities on diffusion mri: From voxels to group studies. *NeuroImage*, 205:116127, 2020. ISSN 1053-8119. doi: 10.1016/j.neuroimage.2019.116127. URL

<https://doi.org/10.1016/j.neuroimage.2019.116127>.

[72] A. Reymbaut, J. P. de Almeida Martins, C. M. W. Tax, F. Szczepankiewicz, D. K. Jones, and D. Topgaard. Resolving orientation-specific diffusion-relaxation features via monte-carlo density-peak clustering in heterogeneous brain tissue, 2020.

[73] Anders Dyhr Sandgaard, Valerij G. Kiselev, Noam Shemesh, and Sune Nørhøj Jespersen. Orientation-Dependent Susceptibility Effects in the Standard Model of Diffusion in White Matter. In *ISMRM Workshop on Diffusion MRI: From Research to Clinic*, page 66, 2022.

[74] “Squashing peanuts and smashing pumpkins”’: How noise distorts diffusion-weighted MR data. *Magnetic Resonance in Medicine*, 52(5):979-993, 2004. doi: 10.1002/mrm.20283. URL

<https://doi.org/10.1002/mrm.20283>.

A. Appendix: Key findings from Tax et al. [21]

In our previous work, we estimated the apparent R_2 -values for intra- and

extra-axonal compartments from the WM SFP data acquired by varying nominal b -values and TEs simultaneously. The acquisition parameters are reproduced in this work in Figure 1A. The compartmental spin-echo signals with associated apparent R_2 -values were included in the compartmental model of diffusion in WM. The latter describes the signal as a convolution of the signal associated with a population of perfectly parallel fibres with a fibre orientation distribution function. The diffusion in the intra- and extra-axonal spaces was described by ‘stick’ and ‘zeppelin’ tensors, respectively.

We then characterised the dependence of the compartmental R_2 -values on WM fibre orientation angle θ w.r.t. \vec{B}_0 :

$$R_2(\theta) = R_{2,\text{iso}} + f(\theta) , \quad (\text{A1})$$

$$f(\theta) = R_{2,\text{aniso}_1} \cdot \sin^2\theta + R_{2,\text{aniso}_2} \cdot \sin^4\theta . \quad (\text{A2})$$

$R_{2,\text{iso}}$ is a θ -independent isotropic component of $R_2(\theta)$, whereas $f(\theta)$ describes the orientation-dependent component. We allowed the corresponding anisotropic coefficients $R_{2,\text{aniso}_{1/2}}$ to be independent, linked, or set to zero, to achieve different variations of this generalised representation. This resulted in a set of the following five representations:

$$R_2(\theta) = R_{2,\text{iso}} , \quad (\text{A3})$$

$$R_2(\theta) = R_{2,\text{iso}} + R_{2,\text{aniso}} \cdot \sin^2 , \quad (\text{A4})$$

$$R_2(\theta) = R_{2,\text{iso}} + R_{2,\text{aniso}} \cdot \sin^4 , \quad (\text{A5})$$

$$R_2(\theta) = R_{2,\text{iso}} + R_{2,\text{aniso}} \cdot \left[1 - \frac{1}{4} (3\cos^2 - 1)^2 \right] , \quad (\text{A6})$$

$$R_2(\theta) = R_{2,\text{iso}} + R_{2,\text{aniso}_1} \cdot \sin^2\theta + R_{2,\text{aniso}_2} \cdot \sin^4\theta . \quad (\text{A7})$$

All of them were used to analyse the data pooled from all SFP voxels and head orientations, while only the first three were applied to analyse data, which were anatomically matched between head orientations using tractometry. We also analysed the R_2 -values estimated by fitting a mono-exponential function to the data obtained at $b = 0$ to compare them to previous studies.

Main results from the pooled data. Intra-axonal R_2 -values were best described by the Eq. A6 with the isotropic component of 12.0 s^{-1} and the magnitude of anisotropy of 0.8 s^{-1} . The AIC of the isotropic representation (Eq. A3) was larger than that of the anisotropic representation with $\Delta\text{AIC} = 76$ and $R_{\text{iso}} = 12.6 \text{ s}^{-1}$. Extra-axonal R_2 -values were best represented by the Eq. A5 with the isotropic component of 17.4 s^{-1} and the magnitude of anisotropy of 2.4 s^{-1} .

The corresponding isotropic representation was not supported with $\Delta\text{AIC} = 838$ and $R_{\text{iso}} = 18.7 \text{ s}^{-1}$.

Main results from the tractometry analysis. Intra-axonal values were best supported by the isotropic representation, while extra-axonal values were best supported by $\sin^4\theta$ -representation with the magnitude of anisotropy of $5.1 \pm 3.0 \text{ s}^{-1}$.